The Astrophysical Journal, 944:164 (9pp), 2023 February 20 https://doi.org/10.3847/1538-4357/acae9e

Evidence for AGN-regulated Cooling in Clusters at z ~ 1.4: A Multiwavelength View of SPT-CL J0607-4448

Megan Masterson[1], Michael McDonald[1], Behzad Ansarinejad[2], Matthew Bayliss[3], Bradford A. Benson[4,5,6], Lindsey E. Bleem[6,7], Michael S. Calzadilla[1], Alastair C. Edge[8], Benjamin Floyd[9], Keunho J. Kim[3], Gourav Khullar[1,10,11], and Taweewat Somboonpanyakul[12]

[1] MIT Kavli Institute for Astrophysics and Space Research, Massachusetts Institute of Technology, Cambridge, MA 02139, USA; mmasters@mit.edu
[2] School of Physics, University of Melbourne, Parkville, VIC 3010, Australia
[3] Department of Physics, University of Cincinnati, Cincinnati, OH 45221, USA
[4] Fermi National Accelerator Laboratory, Batavia, IL 60510-0500, USA
[5] Department of Astronomy and Astrophysics, University of Chicago, Chicago, IL 60637, USA
[6] Kavli Institute for Cosmological Physics, University of Chicago, Chicago, IL 60637, USA
[7] High Energy Physics Division, Argonne National Laboratory, Argonne, IL 60439, USA
[8] Department of Physics, Durham University, Durham, DH1 3LE, UK
[9] Department of Physics and Astronomy, University of Missouri–Kansas City, 5110 Rockhill Road, Kansas City, MO 64110, USA
[10] Department of Astronomy and Astrophysics, University of Chicago, 5640 South Ellis Avenue, Chicago, IL 60637, USA
[11] Kavli Institute for Cosmological Physics, University of Chicago, 5640 South Ellis Avenue, Chicago, IL 60637, USA
[12] Kavli Institute for Particle Astrophysics & Cosmology, P.O. Box 2450, Stanford University, Stanford, CA 94305, USA
Received 2022 July 7; revised 2022 December 12; accepted 2022 December 23; published 2023 February 27

Abstract

We present a multiwavelength analysis of the galaxy cluster SPT-CL J0607-4448 (SPT0607), which is one of the most distant clusters discovered by the South Pole Telescope at $z = 1.4010 \pm 0.0028$. The high-redshift cluster shows clear signs of being relaxed with well-regulated feedback from the active galactic nucleus (AGN) in the brightest cluster galaxy (BCG). Using Chandra X-ray data, we construct thermodynamic profiles and determine the properties of the intracluster medium. The cool-core nature of the cluster is supported by a centrally peaked density profile and low central entropy ($K_0 = 18^{+11}_{-9}$ keV cm^2), which we estimate assuming an isothermal temperature profile due to the limited spectral information given the distance to the cluster. Using the density profile and gas cooling time inferred from the X-ray data, we find a mass-cooling rate $\dot{M}_{\rm cool} = 100^{+90}_{-60}\,M_\odot$ yr^{-1}. From optical spectroscopy and photometry around the [O II] emission line, we estimate that the BCG star formation rate is $\mathrm{SFR}_{[\mathrm{O\,II}]} = 1.7^{+1.0}_{-0.6}\,M_\odot$ yr^{-1}, roughly two orders of magnitude lower than the predicted mass-cooling rate. In addition, using ATCA radio data at 2.1 GHz, we measure a radio jet power of $P_{\rm cav} = 3.2^{+2.1}_{-1.3} \times 10^{44}$ erg s^{-1}, which is consistent with the X-ray cooling luminosity ($L_{\rm cool} = 1.9^{+0.2}_{-0.5} \times 10^{44}$ erg s^{-1} within $r_{\rm cool} = 43$ kpc). These findings suggest that SPT0607 is a relaxed, cool-core cluster with AGN-regulated cooling at an epoch shortly after cluster formation, implying that the balance between cooling and feedback can be reached quickly. We discuss the implications for these findings on the evolution of AGN feedback in galaxy clusters.

Unified Astronomy Thesaurus concepts: Brightest cluster galaxies (181); Galaxy clusters (584); Intracluster medium (858); Radio galaxies (1343); High-redshift galaxy clusters (2007)

1. Introduction

A galaxy cluster contains tens to hundreds of member galaxies (with some reaching over a thousand members) surrounded by hot, ionized plasma called the intracluster medium (ICM), all embedded in a massive dark matter halo that constitutes the majority of the cluster mass. The ICM is the dominant baryonic component of clusters, and it is visible at X-ray wavelengths via bremsstrahlung radiation caused by the motion of charged particles. We often classify galaxy clusters into two main groups: cool-core clusters, in which the central temperature drops and the density increases, and non-cool-core clusters, which have cores that are roughly isothermal. In cool-core clusters, the ICM has short radiative cooling times and should produce massive cooling flows of $\dot{M} \sim$ 100–1000 $M_\odot$ yr^{-1}, in which cold gas condenses out of the hot plasma (see Fabian 1994, for a review). However, such cooling flows are not observed in most systems, with typical star formation rates (SFRs) on the order of ~1% the expected cooling rate (e.g., O'Dea et al. 2008; McDonald et al. 2018) and a lack of cool gas as probed with high-resolution X-ray spectroscopy (e.g., Peterson et al. 2003; Bregman et al. 2006; Peterson & Fabian 2006).

One of the dominant mechanisms that is thought to prevent the rapid cooling of the ICM is mechanical feedback from an active galactic nucleus (AGN) in the brightest cluster galaxy (BCG; e.g., McNamara & Nulsen 2007, 2012; Fabian 2012). In this paradigm, the radio-loud AGN is accreting well below the Eddington limit and launches powerful jets that inject energy into the ICM by inflating bubbles and thus creating X-ray cavities. Observationally, the inflation of these bubbles has been shown to have enough energy to balance the cooling flow in many systems (e.g., Bîrzan 2004; Dunn & Fabian 2006; Rafferty et al. 2006; Hlavacek-Larrondo et al. 2012, 2015). Although AGN feedback is now generally accepted as one of the main heating mechanisms balancing cooling in clusters of galaxies, there are still many open questions, including how the

properties of the ICM and the impact of AGN feedback have evolved over cosmic time.

The study of high-redshift galaxy clusters and cluster evolution has been greatly aided by recent advances in the millimeter/submillimeter regime, whereby the thermal Sunyaev–Zel'dovich (SZ) effect can be used to detect galaxy clusters using their imprint on the cosmic microwave background (Sunyaev & Zeldovich 1972). Millimeter observatories like the Planck satellite (Planck Collaboration et al. 2016), the Atacama Cosmology Telescope (Hilton et al. 2018, 2021), and the South Pole Telescope (SPT; Carlstrom et al. 2011; Bleem et al. 2015, 2020; Huang et al. 2020) have greatly increased the number of detected galaxy clusters at $z > 1$. The SZ selection method is mass-limited, nearly redshift-independent (e.g., Bleem et al. 2015), and independent of the dynamical state of the cluster (e.g., Nurgaliev et al. 2017), allowing for a selection function well-suited for cluster evolution studies. In addition, SZ detection avoids significant bias toward strong cool-core systems (e.g., Lin et al. 2015), which plagues X-ray-detection mechanisms (e.g., Eckert et al. 2011). Similarly, SZ detection also mitigates some biases in optical and infrared detection methods, including bias towards systems with passive, red BCGs.

Uniform X-ray follow-up of SZ-selected clusters has revealed similarity among the ICM thermodynamic properties and the impact of AGN feedback on the ICM from $z \sim 0$ up to $z \sim 1.7$ (e.g., McDonald et al. 2013; Hlavacek-Larrondo et al. 2015; McDonald et al. 2017; Ghirardini et al. 2021; Ruppin et al. 2021). In particular, the density profiles of clusters are consistent with self-similar evolution in the outskirts and with no redshift evolution in the cores (McDonald et al. 2017; Ruppin et al. 2021), indicating consistent nongravitational processes at play in cluster cores responsible for the deviation from self-similarity. Likewise, Hlavacek-Larrondo et al. (2015) found that the power from AGN feedback in cool-core clusters has been roughly constant up to $z \sim 1$. Probing the ICM in the most distant clusters will be a primary focus of next-generation X-ray missions like Athena (Barret et al. 2020). For now, focusing on multiwavelength observations of the most distant clusters allows us to place constraints on the nature of AGN feedback and ICM properties at $z > 1$.

SPT-CL J0607-4448 (hereafter, SPT0607) is one of the most distant SPT clusters discovered to date (Bleem et al. 2015), with a redshift of $z = 1.4010 \pm 0.0028$ as measured by spectroscopic follow-up of cluster members (Khullar et al. 2019). As such, it has been extensively followed up with various observatories and has been studied in the X-ray as part of the SPT-SZ high-z sample (McDonald et al. 2017; Ghirardini et al. 2021). In the optical band, SPT0607 seems to contain two main groups of galaxies, one at $z = 1.401$ and one closer to $z \sim 1.48$. However, the red sequence, dynamics of the cluster members, and spectroscopy of the BCG favor the lower-redshift solution (Khullar et al. 2019; Strazzullo et al. 2019). Finally, the galactic properties of cluster members were investigated in Strazzullo et al. (2019), where they found an overdensity of red galaxies in the cluster, although this overdensity was less prominent than other clusters in their sample (with $1.4 \lesssim z \lesssim 1.7$) despite SPT0607 having the most massive BCG. Our analysis of SPT0607 brings together multiwavelength observations to put together the full picture of this relaxed, cool-core cluster with well-regulated cooling and feedback at such a high redshift.

This work is organized as follows. In Section 2, we outline the multiwavelength data analyzed in this work. We present our results in Section 3, and we discuss the implications of these findings on our understanding of cluster evolution and the AGN feedback process at high redshift in Section 4. Finally, we summarize our findings in Section 5. Throughout this work, we utilize a Lambda cold dark matter (ΛCDM) cosmology with $H_0 = 70$ km s^{-1} Mpc^{-1}, $\Omega_M = 0.3$, and $\Omega_\Lambda = 0.7$. All quoted uncertainties correspond to 68% (1σ) confidence, unless otherwise noted.

2. Observations and Data Reduction

In Figure 1, we show the X-ray, optical/IR, and radio data used in this analysis of SPT0607. On the left and right, we show the Chandra X-ray data and ATCA radio data, respectively, and locate the associated peaks in green (X-ray) and magenta (radio). The center panel shows an RGB image using three Hubble Space Telescope (HST) filters (F140W, F110W, and F814W), with the same locations of the X-ray and radio peaks overplotted. Both the X-ray and radio peak are coincident with the BCG of SPT0607, as expected for a well-regulated cool-core cluster. In the rest of this section, we describe the data and reduction methods used in this paper.

2.1. Chandra X-Ray Observations

SPT0607 was observed with the Chandra ACIS-I instrument for a total of 112.5 ks in 2016 January and February. The details of the observations used in this analysis are provided in Table 1. We reduced and analyzed these data using CIAO (version 4.12; Fruscione et al. 2006) and calibration files from CALDB (version 4.9.2.1). All observations were taken in VFAINT mode, so we applied additional improved background filtering. We detected and removed point sources using the wavdetect tool and sigma-clipped the light curve at 3σ with the lc_clean tool to remove any periods of background flaring from our good time intervals.

At $z = 1.401$ (Khullar et al. 2019), the angular extent of the cluster is relatively small compared to the ACIS-I array, taking up only a single detector chip. Thus, we used an off-source region on the remaining other three detectors to produce the background spectra. We extracted source and background X-ray spectra in the 0.5–7 keV energy range and used XSPEC (version 12.11.1) for spectral fitting. Spectra were grouped to a minimum of one count per bin, and C-statistic minimization was used for fitting (Cash 1979). We used the XSPEC model phabs(apec), where the phabs component accounts for absorption in the Milky Way and the apec model accounts for the emission from the ICM. Abundances were taken from Anders & Grevesse (1989). The absorption column density for the phabs model was free to vary between galactic N_H value, $N_H = 6.78 \times 10^{20}$ cm^{-2} (HI4PI Collaboration et al. 2016), and the galactic $N_{H,tot}$ value, $N_{H,tot} = N_{H\,I} + N_{H_2} = 8.33 \times 10^{20}$ cm^{-2} (Willingale et al. 2013). For the cluster emission, we fixed the redshift to $z = 1.401$ and the metallicity to $Z = 0.3\ Z_\odot$, given the limited data quality.

2.2. Optical and Infrared Photometry

SPT0607 was observed with the HST in four different broadband filters with Proposal IDs 14252 (PI: V. Strazzullo) and 14677 (PI: T. Schrabback). The cluster was observed in the optical to near-IR (rest-frame) with the F606W and F814W

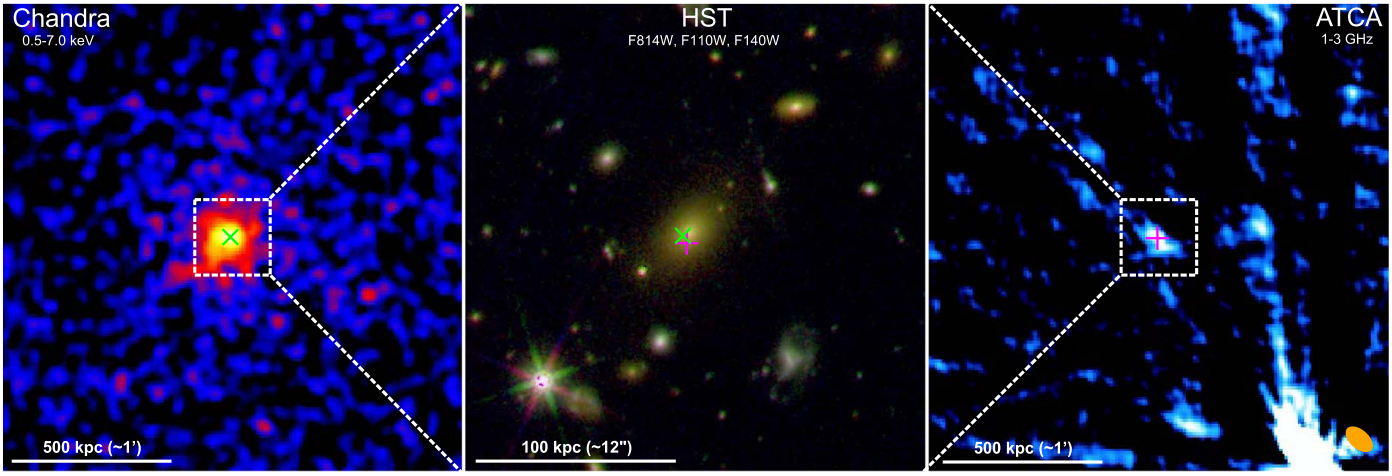

Figure 1. Left: merged Chandra X-ray counts image in the broadband 0.5–7 keV. The image is binned such that each pixel is 0.984 on each side and then smoothed with a Gaussian kernel of four pixels. The green "×" shows the location of the X-ray peak, which we use as the center for all X-ray profiles. Middle: RGB image of SPT0607 using the HST F140W (red), F110W (green), and F814W (blue) filters. The green "×" shows the location of the X-ray peak and the magenta "+" shows the location of the radio peak, both of which are coincident with the BCG of SPT0607. Right: ATCA 2 GHz radio image with the synthesized beam in orange in the lower right corner. The magenta "+" shows the location of the radio peak.

Table 1
Chandra Observation Information

ObsID	Date	Cleaned Exposure Time (ks)
17210	2016-2-4	37.4
17499	2016-1-30	39.3
17500	2016-2-20	17.8
18770	2016-2-22	18.0

filters using the Advanced Camera for Surveys and with the F110W and F140W filters using the Wide Field Camera 3. The data were reduced using the AstroDrizzle package to remove cosmic rays, perform standard data reduction, and combine images. We utilize the HST photometry primarily to understand the optical spectral energy distribution (SED) of the BCG and calibrate our ground-based spectroscopy. The BCG of SPT0607 is undetected in the blue filter, F606W, leading to a 1σ upper limit on the flux of $F_{\lambda,F606W} > 9.1 \times 10^{-20}$ erg s^{-1} cm^{-2} Å^{-1}.

2.3. Optical Spectroscopy

Optical spectra of potential cluster members of SPT0607 were obtained using the Low Dispersion Survey Spectrograph (LDSS-3C) on the 6.5 m Magellan Clay Telescope (Khullar et al. 2019). The VPH-Red grism was used, providing nominal wavelength coverage from 6000–10000 Å. With SPT0607 at a redshift of $z = 1.401$, this wavelength coverage provides access to the [O II] emission line, which was used to estimate the amount of star formation in the BCG. However, these spectra, initially designed for cluster confirmation by measuring the redshift of potential cluster members, were only wavelength-calibrated and not flux-calibrated. Therefore, in order to obtain a line flux for [O II] to estimate SFRs, we utilized the HST photometry to roughly calibrate the spectrum flux. We first measured an equivalent width from the uncalibrated LDSS-3C spectrum and then fit the three-band HST photometry to an SED with an old and a young stellar population (10 Gyr and 10 Myr, respectively) derived from the STARBURST99 models (Leitherer et al. 1999). As the BCG in SPT0607 was undetected in the F606W filter, we used only the F814W, F110W, and F140W photometry measurements from HST to fit the SED, which was constrained to within roughly 10% at the 1σ level around the rest-frame wavelength of [O II] (see Figure 5 and Section 3.3). This provided a measure of the expected continuum flux at the wavelength of [O II], which thus allowed us to convert the equivalent width of the [O II] emission line in the LDSS-3C spectrum to a line flux.

2.4. Radio Observations

SPT0607 was observed with the ATCA in the 6A configuration in the 1–3 GHz band on 2016 August 20 in seven 20 minute visits spread evenly over an 8.5 hr period. These data provide a beam of 6″ × 3.″5 at 2 GHz. The data were reduced with the 05/21/2015 release of the Miriad software package (Sault et al. 1995). The phase calibrator 0647-475 was used to create the radio maps, with some multifaceting, but no self-calibration was necessary. The rms value for the resulting image is 23 μJy with a dynamic range of ~3000, ensuring sensitivity to extended emission.

3. Results

3.1. Intracluster Medium Properties and Thermodynamic Profiles

In this section, we present the results of the X-ray data analysis whereby we measure the properties of the ICM in SPT0607. We are focused on the core properties of SPT0607, where the impact of AGN feedback is most prevalent, and hence we measured our radial profiles with respect to the X-ray peak location, as marked in the left and middle panels of Figure 1. As has been noted previously (e.g., McDonald et al. 2013; Sanders et al. 2018; Ruppin et al. 2021), using a center based on the large-scale X-ray centroid, as was done in McDonald et al. (2017) and Ghirardini et al. (2021), gives a slightly different profile and leads to lower central density and higher central entropy. Additionally, we note that, given the relatively high number of counts from SPT0607 (~700), our peak location is robust to variations due to noise (e.g., Ruppin et al. 2021).

Due to the high redshift of the source, we make a few conservative assumptions with respect to the temperature profile of the cluster. We first assume that the temperature profile is isothermal, where the temperature is a core-excised temperature measured within a radius $(0.15-1)R_{500}$, using $R_{500} = 0.56$ Mpc from McDonald et al. (2017). Although this is likely a poor assumption for the true nature of the temperature profile in SPT0607, it provides a strong upper bound on many of our measured thermodynamic properties. In reality, we believe that the cluster has a strong cool core due to the excess surface brightness, radio jet, and lack of significant star formation features in the BCG. We then show in the remainder of this section that we can still recover the features of a strong cool core even with this assumption of an isothermal temperature profile, providing compelling evidence for the cool-core nature of this system. After showing that SPT0607 does indeed host a cool core, we also assume a standard cool-core temperature profile (Vikhlinin et al. 2006), scaled to the global, core-excised temperature, to obtain a better estimate of the central thermodynamic properties.

3.1.1. Global Temperature Measurement

As detailed in Section 2.1, we fit the cluster X-ray spectrum in the core-excised region with the simple model phabs (apec) for cluster emission, with the redshift fixed at $z = 1.401$. Cluster metallicity is typically constrained by the highly ionized Fe K-shell lines in X-ray spectra of the ICM, but it is poorly constrained in our fits, given the high redshift of SPT0607. Thus, we fixed the metallicity at $Z = 0.3\ Z_e$, motivated by detailed low-redshift studies, which find that the average cluster metallicity is roughly a third of the solar value (e.g., Mushotzky & Loewenstein 1997; De Grandi & Molendi 2001; Urban et al. 2017), as well as recent metallicity evolution studies, which show little evolution in the cluster metallicity out to $z \sim 1$ (e.g., McDonald et al. 2016a; Flores et al. 2021). The ICM metallicity has been shown to have a weak dependence on temperature (e.g., Fukazawa et al. 1998), and hence this choice likely has little impact on our measured global temperature. Following the methodology outlined in Section 2.1, we find a core-excised temperature $\langle kT\rangle = 6.75^{+2.14}_{-1.51}$ keV. Using the higher redshift value for SPT0607 of $z = 1.48$ for the cluster redshift (see Section 1), we measure a slightly higher core-excised temperature $\langle kT\rangle = 8.07^{+6.30}_{-2.76}$ keV, but this is consistent with our initial estimate within 1σ uncertainty. Using both Chandra and XMM-Newton data, Ghirardini et al. (2021) found a temperature of $T_0 = 6.0 \pm 0.8$ keV when fitting a Vikhlinin cool-core temperature profile, which is consistent with our measurement when considering the differences in the temperature estimates (Vikhlinin et al. 2006).

3.1.2. Emission Measure and Density Profiles

To derive an emission measure from the X-ray data, we extracted a spectrum from each observation in radial bins. We used extraction bins with outer radii defined by

$$r_{\mathrm{out},i} = (a + bi + ci^2 + di^3)R_{500}, \quad (1)$$

where the constants a, b, c, and d are as defined in McDonald et al. (2017), $R_{500} = 560$ kpc (McDonald et al. 2017), and $i = 1, 2, K, 17$. We use fewer radial annuli than in McDonald et al. (2017), due to poor signal-to-noise in the cluster outskirts for SPT0607. In each radial bin, we fit the spectrum for all four observations simultaneously, with all parameters tied across all observations. To derive an emission measure, we simply fix the temperature to the global, core-excised temperature previously described and fit only to the normalization of the apec model. The normalization of the apec model has astrophysical meaning and is given by

$$\mathrm{norm} = \frac{10^{-14}}{4\pi[D_A(1+z)]^2}\int n_e n_H dV, \quad (2)$$

where D_A is the angular distance to the source in units of centimeters, n_e is the electron density in cubic centimeters, and n_H is the hydrogen density in cubic centimeters. Then, by assuming a spherical geometry, the normalization can be related to the emission measure, which is given by

$$\mathrm{EM} = \int n_e n_H dl, \quad (3)$$

where the integral here is along the line of the sight through the cluster. Thus, we can use the apec normalization to obtain the emission measure for each radial bin. Because the normalization measurement is dependent on the temperature we use, we also account for the uncertainty in the temperature measurement by including an additional 10% uncertainty on each apec normalization measurement (the average difference between the normalization at $\langle kT\rangle$ and the normalization at $\langle kT\rangle \pm 1\sigma$ for the isothermal temperature).

To fit the emission measure, we use the modified β model (Vikhlinin et al. 2006), whereby the density is given by

$$n_e n_H = n_0^2 \frac{(r/r_c)^{-a}}{(1+r^2/r_c^2)^{3b-a/2}} \frac{1}{(1+r^3/r_s^3)^{\gamma/3}}, \quad (4)$$

where n_0 is the central density, r_c and r_s are scaling radii for the cluster core and outskirts, and r is the radial coordinate. This model for the density is then projected and integrated numerically along the line of sight to create an emission measure model. We utilize the Markov Chain Monte Carlo (MCMC) implementation emcee from Foreman-Mackey et al. (2013) to perform the fitting. We use uniform priors on all parameters and a Gaussian likelihood, given by

$$\mathcal{L} = -\frac{1}{2}\chi^2 = -\frac{1}{2}\sum_{i=1}^{N}\left(\frac{\mathrm{EM}_{\mathrm{measured}} - \mathrm{EM}_{\mathrm{model}}}{\sigma_{\mathrm{EM}}}\right)^2, \quad (5)$$

where σ_{EM} are our errors on the emission measure. We first maximize this likelihood function for our data and then use the maximum-likelihood parameters with some scatter as our initial position for the walkers in the MCMC chain. We run the chain with 32 walkers, each for 5×10^5 chain steps after a burn length of 5×10^4 chain steps (which is significantly longer than the integrated autocorrelation time of the resulting chain). The resulting fit to the emission measure is shown in the left panel of Figure 2.

We can easily turn our emission measure fit into a gas density profile for the cluster, as we have fit parameters directly related to the density via Equation (4). For an ionized plasma with a metallicity of 0.3 Z_e, n_e and n_H are related via $n_e = Zn_H$, where $Z = 1.199$ is the average nuclear mass. Likewise, the total gas density of the system can be described by $\rho = m_p n_e A/Z$, where m_p is the mass of a proton and $A = 1.397$ is the average

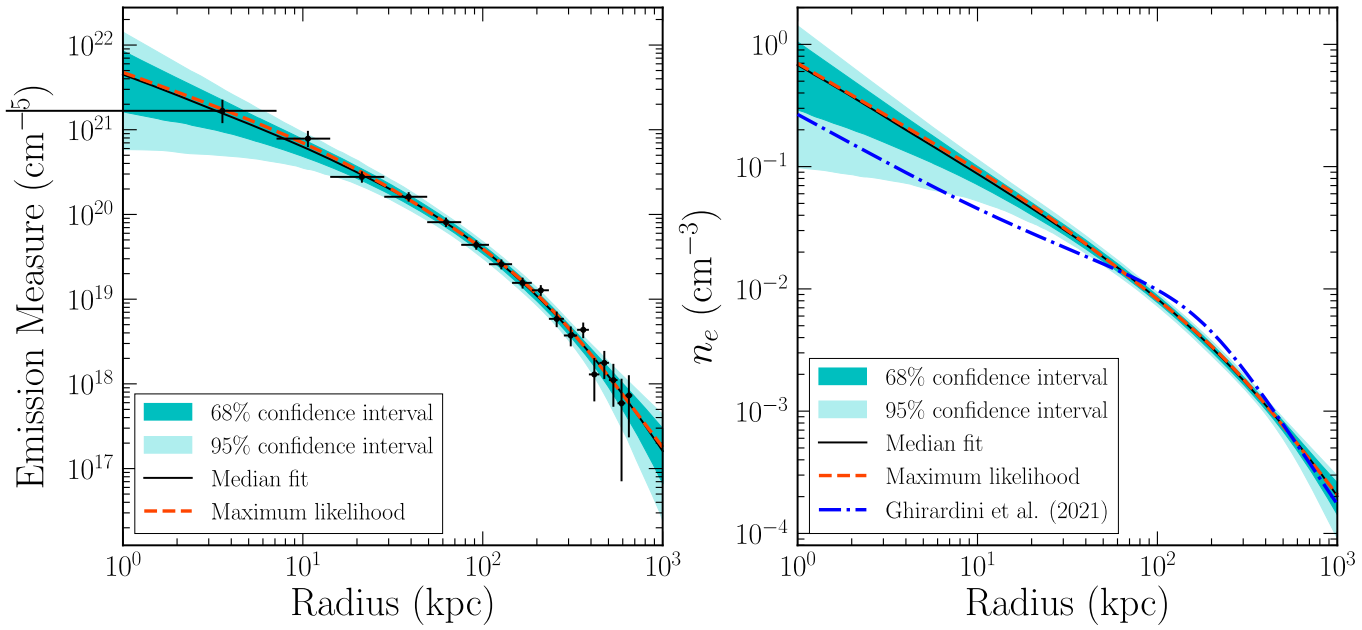

Figure 2. Left: the emission measure fit for SPT0607. The emission measure is computed by using the APEC normalization in each of the imaging bins and fitting a projected density profile by integrating along the line of sight through the cluster. The red dashed line shows the maximum-likelihood fit using the Gaussian likelihood given in Equation (5). The profile with median fit parameters from the MCMC fit is shown in black, and the confidence interval from the MCMC chain at each radius for 68% and 95% confidence is shown in the shaded regions. Right: the density profile for SPT0607 computed from the emission measure fit. The maximum-likelihood profile is again shown in red, the median MCMC profile is shown in black, and the 68% and 95% confidence intervals are shown in the shaded regions. The comparison to the density profile from Ghirardini et al. (2021) is shown in blue. The discrepancy between the two profiles in the core is likely due to our different choice of center (see Section 3.1.2)

nuclear charge. Our density profile is shown in the right panel of Figure 2, with a comparison to the density profile from Ghirardini et al. (2021), which utilizes both Chandra and XMM-Newton data. Ghirardini et al. (2021) use a large-scale centroid to compute their radial profiles, whereas we choose an X-ray peak approach to capture the core properties. We find decent agreement at the majority of the cluster radii, although our profile predicts a larger overdensity in the cluster core. When using a centroid-based approach (i.e., the Ghirardini et al. (2021) center), we find better agreement between the two profiles, suggesting that the discrepancy in Figure 2 is due to our choice of using the X-ray peak as the cluster center rather than the large-scale centroid.

3.1.3. Entropy Profile

With the density profile for the cluster, we derive an entropy profile, which can both give us insight into the cool-core nature of the cluster and trace the thermodynamic history of the ICM (Cavagnolo et al. 2009). Cluster entropy is defined as

$$K = \frac{kT}{n_e^{2/3}}. \quad (6)$$

Assuming an isothermal temperature profile provides an upper limit on the true entropy profile in the core of the cluster. Figure 3 shows the entropy profile for SPT0607 using the isothermal temperature profile described in Section 3.1.1 and discretizing the entropy in the same bins as we used to measure the emission measure. We find good agreement in the cluster outskirts with the self-similar $K \propto R^{1}$ expectation (Voit et al. 2005). In the center, we find slight excess entropy compared to the self-similar expectation, with a central entropy of $K_0 = 18^{+11}_{-9}$ keV cm^2 in the smallest bin ($r \approx 10$ kpc). Thus,

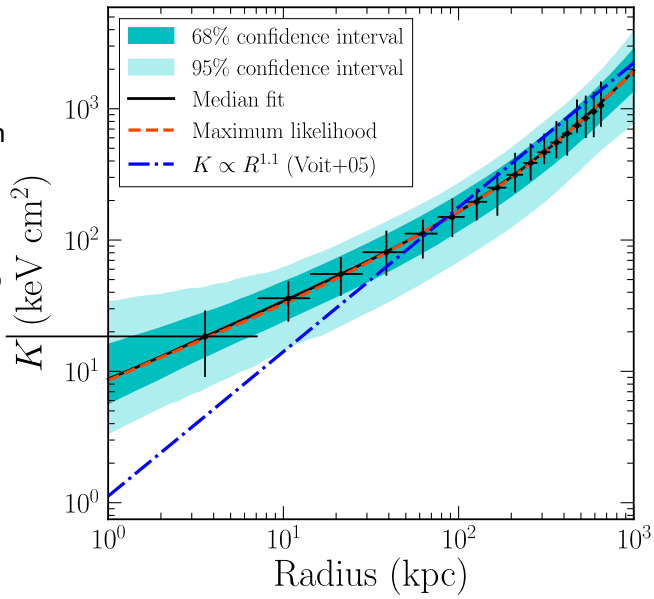

Figure 3. The entropy profile for SPT0607, computed from the derived density profile and an isothermal temperature profile. The analytic profile has been discretized in the same binning scheme used to fit the emission measure data. We find a low-entropy core and good agreement in the cluster outskirts with the expected $K \propto R^{1.1}$ relation from Voit et al. (2005).

even with the most conservative assumption of an isothermal temperature profile, we still recover a low-entropy core, consistent with the central entropy in the strong cool cores in the sample from Hudson et al. (2010) ($K_0 \lesssim 22$ keV cm^2). This indicates that SPT0607 is indeed a strong cool-core cluster.

To obtain a more accurate estimate of the central entropy, we also computed the entropy profile assuming that the

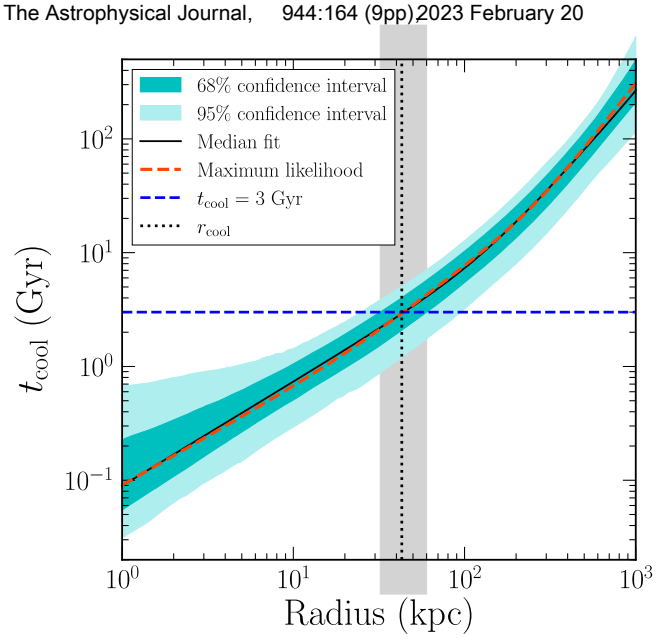

Figure 4. The cooling time profile for SPT0607, computed assuming an isothermal temperature profile and density profiles derived in Section 3.1.2. The radius corresponding to t_{cool} = 3 Gyr is shown with a blacked dotted line, with the corresponding 68% confidence interval shown in gray.

temperature followed the Vikhlinin et al. (2006) cool-core profile. Under this assumption, we find a central entropy $K_0 = 10^{+3}_{-6}$ keV cm^{-2}, which is again consistent with a strong cool core in SPT0607.

3.1.4. Cooling Time

The last key thermodynamic quantity that we compute is the cooling time, which is used to estimate r_{cool} so that we can measure a mass-cooling rate to compare with other indicators of cooling to get an idea of the suppression caused by AGN feedback. We compute the cooling time for the cluster using

$$t_{cool} = \frac{3}{2}\frac{(n_e + n_H)kT}{n_e n_H \Lambda(T,Z)}, \quad (7)$$

where $\Lambda(T, Z)$ is the cooling function for an astrophysical plasma at a temperature T and metallicity Z, which we tabulate from Sutherland & Dopita (1993) for the closest temperature and metallicity for SPT0607. The cooling time profile we derive with an isothermal temperature profile is shown in Figure 4.

Using this cooling time profile, we measure a cooling radius of $r_{cool} = 43^{+17}_{-11}$ kpc, which is defined as the radius at which the cooling time is equal to 3 Gyr. A cooling time of 3 Gyr was chosen because it has been shown to contain the most extended tracers of thermal instabilities in the ICM (e.g., McDonald et al. 2010, 2011). To obtain a mass-cooling rate, we then integrate the gas density profile to within the cooling radius and compute the mass-cooling rate using

$$\dot{M}_{cool} = \frac{M_{gas}(r < r_{cool})}{3\ \mathrm{Gyr}}. \quad (8)$$

From this, we estimate from the X-ray analysis that the expected mass-cooling rate is $\dot{M}_{cool} = 100^{+90}_{-60}\ M_\odot$ yr^{-1}. Similarly to the central entropy, we also compute this value using a scaled version of the universal cool-core temperature profile and find consistent mass-cooling rates under that assumption.

3.2. Radio Power

We utilize ATCA 2.1 GHz observations of SPT0607 to determine the total radio power associated with the BCG in SPT0607. The jet from the BCG is unresolved, and we measure an integrated flux using CASA (McMullin et al. 2007) of $S_{2.1\ GHz} = 0.23 \pm 0.11$ mJy within an ovular aperture equal to the beam size centered on the radio peak. This corresponds to a 2.1 GHz radio luminosity of $L_{2.1\ GHz} = (2.3 \pm 1.1) \times 10^{24}$ W Hz^{-1}. We then estimate the radio power using

$$P_{\nu_0} = 4\pi D_L^2 (1+z)^{\alpha-1} S_{\nu_0} \nu_0, \quad (9)$$

from Cavagnolo et al. (2010), where ν_0 is the observed frequency (2.1 GHz), S_{ν_0} is the flux density at the observed frequency, D_L is the luminosity distance, and α is the spectral index. Since we only have data at one frequency from ATCA, we cannot measure the spectral index, but instead adopt a typical value for extragalactic radio galaxies of α = 0.8 as in Cavagnolo et al. (2010). Using a spectral index of α = 0.8, we find a radio power of $P_{2.1\ GHz} = (4.8 \pm 2.4) \times 10^{40}$ erg s^{-1}.

To compare the power of the radio jet in the BCG to the amount of cooling expected in the ICM, we use the scaling relation from Cavagnolo et al. (2010) to convert the measured radio power to a jet power. We first use the same spectral index to convert the observed 2.1 GHz power to a 1.4 GHz power, which can then be directly converted to jet power using Equation (1) of Cavagnolo et al. (2010) given by

$$\log P_{cav} = (0.75 \pm 0.14) \log P_{1.4} + (1.91 \pm 0.18), \quad (10)$$

where P_{cav} is in units of 10^{42} erg s^{-1} and $P_{1.4}$ is in units of 10^{40} erg s^{-1}. We find a jet power of $P_{cav} = 3.2^{+2.1}_{-1.3} \times 10^{44}$ erg s^{-1} using this scaling relation. To compare the heating from the radio jet to the cooling of the ICM, we compute the X-ray cooling luminosity of the ICM within r_{cool}, using our derived value of r_{cool} from Section 3.1.4. We find an unabsorbed X-ray cooling luminosity of $L_{cool} = 1.9^{+0.2}_{-0.5} \times 10^{44}$ erg s^{-1} in the 0.01–100 keV band, which is consistent with the radio jet power within 1σ confidence. This is consistent with the radio BCG power versus X-ray cooling luminosity found in a large sample of low-redshift clusters in Hogan et al. (2015), as well as with the lack of a significant redshift evolution in P_{cav}/L_{cool} for clusters out to z ~ 1.3 in Ruppin et al. (2022). The implications of these findings on the regulation of cooling in SPT0607 by radio-mode AGN feedback are discussed further in Section 4.

3.3. Regulated Star Formation in the Brightest Cluster Galaxy

Using the LDSS-3C optical spectrum from the Magellan Clay telescope, we estimate the SFR in the BCG by measuring a luminosity of the [O II] λλ3727, 3729 Å doublet. The [O II] emission feature is a useful indicator of star formation (e.g., Kennicutt 1998; Kewley et al. 2004), especially in the high-redshift universe, because it has a similar ionization energy to hydrogen, but unlike the Hα transition, it is not redshifted out of the optical band. The [O II] emission traces warm gas with T ~ 10^4 K around young O and B stars, thus tracing instantaneous star formation on timescales on the order of

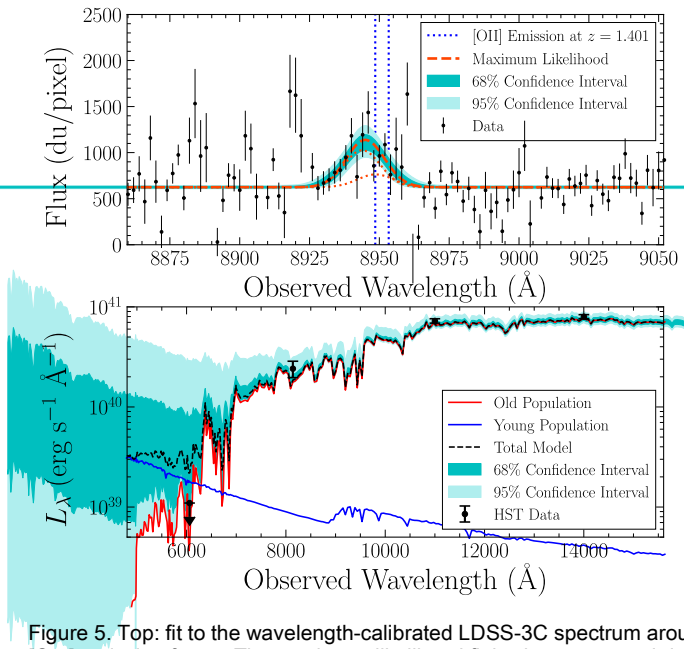

Figure 5. Top: fit to the wavelength-calibrated LDSS-3C spectrum around the [O II] emission feature. The maximum-likelihood fit is shown as a red dashed line, with the two individual Gaussian components shown with red dotted lines. Confidence intervals are shown in green. The observed wavelength of the [O II] doublet is shown with blue dotted lines. We allow for some systematic offset from the observed wavelength to account for motion within the cluster. Bottom: fit to the three-band HST photometry using a simple young and old stellar population model from STARBURST99 (Leitherer et al. 1999). The total model is shown in black, with confidence intervals in green. The young and old stellar population contributions are shown in blue and red, respectively. A 1σ upper bound from the F606W filter is also shown, although this is not used in the fitting procedure. The SED fit is used to obtain a continuum flux at the wavelength of [O II], with which we can combine the equivalent width measurement from the top panel to determine the [O II] line flux.

~10 Myr. However, SFRs derived from [O II] emission line are more dependent on dust, metallicity, and ionization than other tracers like Hα, UV, and far-IR luminosities (e.g., Rosa-Gonzalez et al. 2002; Kewley et al. 2004; Moustakas 2006), which we cannot accurately determine with current data on SPT0607. AGN can also excite [O II] in the nuclei of galaxies, but the AGN in SPT0607 is radiatively inefficient and weak in X-ray emission. Thus, we do not expect the central AGN to be contributing significantly to the [O II] emission in SPT0607, and we can safely attribute the majority of the [O II] emission to star formation.

We fit the LDSS-3C spectrum within 100 Å on either side of the expected [O II] emission feature with a constant to estimate the continuum and doublet Gaussian feature for the [O II] line. We fix the redshift at $z = 1.401$ for the cluster, and allow the line centers to vary within 500 km s^{-1} of the atomic value in order to account for peculiar motions in the cluster. We restrict the width of the line to be less than 500 km s^{-1}, to account for turbulent motions broadening the line. We tie the widths of the two Gaussian components together and allow their line ratio to be free. We use the emcee package (Foreman-Mackey et al. 2013) with a Gaussian likelihood and uniform, uninformative priors to fit the spectrum using an MCMC approach with 32 walkers, 50,000 chain steps per walker, and a burn length of 5000 chain steps per walker (which is significantly longer than the integrated autocorrelation time of the resulting chain). The result of the fit is shown in the top panel of Figure 5. We detect a relatively weak emission feature in [O II] with a velocity

Table 2
Summary of Cluster and BCG Properties

BCG Property	Value
Central entropy	$K_0 = 18^{+11}_{-9}$ keV cm^2
X-ray mass-cooling rate	$\dot{M}_{\rm cool} = 100^{+90}_{-60}\ M_\odot$ yr^{-1}
X-ray cooling luminosity	$L_{\rm cool} = 1.9^{+0.2}_{-0.5} \times 10^{44}$ erg s^{-1}
Radio jet power	$P_{\rm cav} = 3.2^{+2.1}_{-1.3} \times 10^{44}$ erg s^{-1}
Star formation rate	$1.7^{+1.0}_{-0.6}\ M_\odot$ yr^{-1}

offset of $v = -200 \pm 60$ km s^{-1}, a line width of 230 ± 40 km s^{-1}, and a rest-frame equivalent width (EW) of $EW_{[OII]} = 6.0 \pm 0.9$ Å. This equivalent width is then turned into a line flux using the flux-calibrated HST photometry to model the continuum SED, as shown in the bottom panel of Figure 5 and detailed in Section 2.3.

From this calibration, we measure an [O II] luminosity of $L_{[O\,II]} = 1.3^{+0.3}_{-0.2} \times 10^{41}$ erg s^{-1}, which has not been corrected for extinction. We account for extinction by folding in uncertainty on E(B − V) by assuming a uniform distribution between E(B − V) = 0 (i.e., dust-free) and E(B − V) = 0.3. Using Equations (10) and (17) of Kewley et al. (2004), we convert our observed [O II] luminosity to an SFR (assuming a solar value of log(O/H) + 12 = 8.9). From our MCMC chains fitting the line and folding in the uniform distribution of E(B − V), we obtain an extinction-corrected SFR of $SFR_{[O\,II]} = 1.7^{+1.0}_{-0.6}\ M_\odot$ yr^{-1}. This value is more than two orders of magnitude lower than the cooling rate we measure in the X-ray band, indicating that the cooling in SPT0607 is well-regulated by AGN feedback. Likewise, this SFR is comparable to low-redshift samples of BCGs with little ongoing star formation as measured with Hα and other SFR indicators (e.g., Crawford et al. 1999; McDonald et al. 2010). This thus adds to the evidence that SPT0607 is a high-redshift analog of the large population of relaxed, low-redshift clusters with well-regulated star formation and ICM cooling by AGN feedback.

4. Discussion

From the analysis of X-ray, optical, and radio observations, SPT0607 clearly hosts a strong cool core with AGN feedback offsetting the cooling from the ICM, as is commonplace in low-redshift galaxy clusters. Table 2 gives an overview of the properties of the cluster and BCG derived in this work, highlighting the low central entropy, similarity of the radio cavity power and cooling luminosity, and the SFR that is ~1% of the predicted mass-cooling rate. In the remainder of this section, we discuss the implications that these findings have on our understanding of high-redshift clusters and the evolution of AGN feedback.

4.1. Constraints on the Onset of Radio-mode Feedback

At low redshifts, radio-mode AGN feedback, whereby the central AGN accretes mass at a low rate and launches radio jets that deposit large amounts of mechanical energy into the ICM, is the main mechanism by which runaway ICM cooling is prevented in cool-core clusters (e.g., Bîrzan 2004; Dunn & Fabian 2006; Rafferty et al. 2006). Through multiwavelength observations, we have shown that SPT0607 has well-regulated radio-mode feedback from its BCG, and to our knowledge, it is the highest-redshift cluster with these properties known to date.

As such, it provides one of the strongest constraints to date on the onset of AGN feedback in galaxy clusters.

Simulations and theoretical models of the evolution of AGN feedback and supermassive black hole growth suggest that, on average, AGN in cluster environments should transition from quasar-mode feedback at early times, where the black hole is accreting at higher rates and the accretion process is radiatively efficient, to radio-mode feedback at late times (e.g., Churazov et al. 2005; Croton et al. 2006). Recent simulations suggest that this transition should take on the order of 1–2 Gyr to occur in BCGs in cool-core clusters (e.g., Qiu et al. 2019). Indeed, at low redshifts, only on the order of 1%–2% of clusters are observed to have an X-ray bright central AGN, which is expected for radiatively efficient accretion in the BCG and quasar-mode feedback (e.g., Green et al. 2017; Somboonpanyakul et al. 2021). SPT0607 has well-regulated radio-mode feedback from its BCG, suggesting that the radio-mode feedback must be present and a dominant form of AGN feedback in some clusters out to at least z = 1.4. Whether this is the dominant mechanism of feedback in most high-redshift systems is a question that still remains to be answered with a more complete sample of radio and X-ray observations of high-redshift clusters. However, we can use SPT0607 to place constraints on the minimum redshift at which AGN feedback must have turned on in clusters; under the assumption that BCGs are dominated by radiatively efficient accretion during the first 1–2 Gyr (Qiu et al. 2019), the lowest redshift at which the AGN feedback process could have begun in SPT0607 is $z \sim 1.9 - 2.6$.

Previously, studies of X-ray cavities from jet-powered bubbles in the ICM have shown there is little evolution in the properties of radio-mode feedback from the local universe back to $z \sim 0.8$ (Hlavacek-Larrondo et al. 2012, 2015). Additionally, the discovery of more distant cool-core clusters with central radio sources capable of balancing ICM cooling, such as WARP J1415.1+3612, have extended these findings out to $z \sim 1$ (Santos et al. 2012). With SPT0607, we can extend this relation even further out to $z = 1.4$. However, it is still unclear when radio-mode feedback was established in galaxy clusters and how the fraction of clusters with well-regulated AGN feedback has evolved out to high redshifts. The next-generation X-ray observatories will target this question by probing the ICM in the most distant clusters, with the ability to detect cluster emission out to $z \sim 2 - 3$ (Barret et al. 2020). With many more systems, we will be able to get a better handle on the evolution of radio-mode feedback and the AGN duty cycle in high-redshift clusters. For now, at $z = 1.401$, SPT0607 provides the furthest constraint on the onset of radio-mode feedback in cool-core clusters.

4.2. Star Formation in Brightest Cluster Galaxies at High Redshift

Star formation in the BCGs in cool-core clusters is a critical piece of the AGN feedback process, as it acts as a probe of the balance between heating by AGN feedback and cooling in the ICM. Various works have found that both the SFR and specific SFR of BCGs increase as a function of increasing redshift (e.g., Webb et al. 2015; McDonald et al. 2016b; Bonaventura et al. 2017). However, the nature of star-forming BCGs seems to have changed with redshift. In particular, McDonald et al. (2016b) found that there was a transition in the fuel supply of the BCG, namely that high-redshift clusters out to $z \sim 1.2$ with highly star-forming BCGs were almost always disturbed clusters. This suggests that gas-rich mergers are responsible for runaway cooling and star formation in high-redshift systems, rather than cooling flows from a lack of heating from AGN feedback, as was recently observed in the $z \sim 1.7$ system SpARCS1049 (Hlavacek-Larrondo et al. 2020). However, at low redshifts, star-forming BCGs are predominantly found in relaxed systems, indicating that star formation in BCGs at low redshifts is commonly driven by cooling of the ICM and regulated by AGN feedback. With multiwavelength observations of SPT0607, we have found that this high-redshift, relaxed cluster hosts a BCG with very little star formation. The BCG also shows no noticeable morphological features in the three-band HST images that suggest any recent mergers or interactions. These findings thus agree with the idea of a transitioning fuel supply for BCG star formation at high redshift, where the majority of the fuel for star formation in high-redshift systems comes from gas-rich mergers as clusters are assembling. SPT0607 supports this picture out to $z \sim 1.4$ and suggests that the early onset of AGN feedback provides sufficient heating to offset direct cooling from the ICM into stars at high redshift.

5. Summary

We have presented a multiwavelength analysis of one of the most distant SPT-selected clusters, SPT0607 at a redshift of $z = 1.401$. Through analysis of Chandra X-ray data, we found that SPT0607 has a strong cool core, as evidenced by both an increase in central gas density and a low-entropy core as measured from the X-ray peak. These results follow from our conservative assumption of an isothermal temperature profile; in reality, we expect the central temperature of SPT0607 to drop in the center, which gives an even lower-entropy core when assumed.

As shown in Figure 1, the core of SPT0607 is coincident with the BCG, which harbors a radio jet detected with ATCA at 2.1 GHz. Despite having a dense and cool core, we measure an SFR in the BCG of SPT0607 of $\mathrm{SFR}_{[\mathrm{OII}]} = 1.7^{+1.0}_{0.6}\ M_\odot\ \mathrm{yr}^{-1}$ using measurements of the [O II] emission line from optical spectroscopy with the LDSS-3C instrument on the 6.5 m Magellan Clay telescope. This SFR is roughly 1% of the expected mass-cooling rate of the ICM, $\dot{M}_{\mathrm{cool}} = 100^{+90}_{-60}\ M_\odot\ \mathrm{yr}^{-1}$ from our X-ray measurements. Similarly, we measure a cavity power from the radio jet of $P_{\mathrm{cav}} = 3.2^{+2.1}_{1.3} \times 10^{44}$ erg s^{-1}, which is consistent with the X-ray cooling luminosity. This indicates that the BCG in SPT0607 is providing radio-mode feedback to offset the cooling from the ICM. This phenomenon is commonplace at low redshift, but as one of the most distant clusters known to date, the regulation of cooling and AGN feedback in SPT0607 gives the strongest constraints on the onset of radio-mode AGN feedback in galaxy clusters to date.

The South Pole Telescope program is supported by the National Science Foundation (NSF) through grants PLR-1248097 and OPP-1852617. Partial support is also provided by the NSF Physics Frontier Center grant PHY-1125897 to the Kavli Institute of Cosmological Physics at the University of Chicago, the Kavli Foundation, and the Gordon and Betty Moore Foundation through grant GBMF#947 to the University of Chicago. Argonne National Laboratory's work was supported by the U.S. Department of Energy, Office of

Science, Office of High Energy Physics, under contract DE-AC02-06CH11357. The Melbourne group acknowledges support from the Australian Research Council's Discovery Projects scheme (DP200101068). All of the HST data used in this paper can be found in MAST: 10.17909/e40m-z102.

Facilities: CXO, HST, Magellan, ATCA, NSF/US Department of Energy 10 m South Pole Telescope (SPT-SZ).

Software: CIAO (Fruscione et al. 2006), XSPEC (Arnaud 1996), CASA (McMullin et al. 2007), STARBURST99 (Leitherer et al. 1999), Astropy (Astropy Collaboration et al. 2013, 2018), Matplotlib (Hunter 2007), NumPy (van der Walt et al. 2011).

ORCID iDs

Megan Masterson https://orcid.org/0000-0003-4127-0739
Michael McDonald https://orcid.org/0000-0001-5226-8349
Behzad Ansarinejad https://orcid.org/0000-0002-6443-3396
Matthew Bayliss https://orcid.org/0000-0003-1074-4807
Bradford A. Benson https://orcid.org/0000-0002-5108-6823
Lindsey E. Bleem https://orcid.org/0000-0001-7665-5079
Michael S. Calzadilla https://orcid.org/0000-0002-2238-2105
Alastair C. Edge https://orcid.org/0000-0002-3398-6916
Benjamin Floyd https://orcid.org/0000-0003-4175-571X
Keunho J. Kim https://orcid.org/0000-0001-6505-0293
Gourav Khullar https://orcid.org/0000-0002-3475-7648
Taweewat Somboonpanyakul https://orcid.org/0000-0003-3521-3631

References

Anders, E., & Grevesse, N. 1989, GeoCoA, 53, 197
Arnaud, K. A. 1996, in ASP Conf. Ser. 101, Astronomical Data Analysis Software and Systems V, ed. G. H. Jacoby & J. Barnes (San Francisco, CA: ASP), 17
Astropy Collaboration, Price-Whelan, A. M., Sipőcz, B. M., et al. 2018, AJ, 156, 123
Astropy Collaboration, Robitaille, T. P., Tollerud, E. J., et al. 2013, A&A, 558, A33
Barret, D., Decourchelle, A., Fabian, A., et al. 2020, AN, 341, 224
Bîrzan, L., Rafferty, D. A., McNamara, B. R., Wise, M. W., & Nulsen, P. E. J. 2004, ApJ, 607, 800
Bleem, L. E., Bocquet, S., Stalder, B., et al. 2020, ApJS, 247, 25
Bleem, L. E., Stalder, B., de Haan, T., et al. 2015, ApJS, 216, 27
Bonaventura, N. R., Webb, T. M. A., Muzzin, A., et al. 2017, MNRAS, 469, 1259
Bregman, J. N., Fabian, A. C., Miller, E. D., & Irwin, J. A. 2006, ApJ, 642, 746
Carlstrom, J. E., Ade, P. A. R., Aird, K. A., et al. 2011, PASP, 123, 568
Cash, W. 1979, ApJ, 228, 939
Cavagnolo, K. W., Donahue, M., Voit, G. M., & Sun, M. 2009, ApJS, 182, 12
Cavagnolo, K. W., McNamara, B. R., Nulsen, P. E. J., et al. 2010, ApJ, 720, 1066
Churazov, E., Sazonov, S., Sunyaev, R., et al. 2005, MNRAS, 363, L91
Crawford, C. S., Allen, S. W., Ebeling, H., Edge, A. C., & Fabian, A. C. 1999, MNRAS, 306, 857
Croton, D. J., Springel, V., White, S. D. M., et al. 2006, MNRAS, 365, 11
De Grandi, S., & Molendi, S. 2001, ApJ, 551, 153
Dunn, R. J. H., & Fabian, A. C. 2006, MNRAS, 373, 959
Eckert, D., Molendi, S., & Paltani, S. 2011, A&A, 526, A79
Fabian, A. C. 1994, ARA&A, 32, 277
Fabian, A. C. 2012, ARA&A, 50, 455
Flores, A. M., Mantz, A. B., Allen, S. W., et al. 2021, MNRAS, 507, 5195
Foreman-Mackey, D., Hogg, D. W., Lang, D., & Goodman, J. 2013, PASP, 125, 306
Fruscione, A., McDowell, J. C., Allen, G. E., et al. 2006, Proc. SPIE, 6270, 62701V
Fukazawa, Y., Makishima, K., Tamura, T., et al. 1998, PASJ, 50, 187
Ghirardini, V., Bulbul, E., Kraft, R., et al. 2021, ApJ, 910, 14
Green, T. S., Edge, A. C., Ebeling, H., et al. 2017, MNRAS, 465, 4872
HI4PI Collaboration, Ben Bekhti, N., Flöer, L., et al. 2016, A&A, 594, A116
Hilton, M., Hasselfield, M., Sifón, C., et al. 2018, ApJS, 235, 20
Hilton, M., Sifón, C., Naess, S., et al. 2021, ApJS, 253, 3
Hlavacek-Larrondo, J., Fabian, A. C., Edge, A. C., et al. 2012, MNRAS, 421, 1360
Hlavacek-Larrondo, J., McDonald, M., Benson, B. A., et al. 2015, ApJ, 805, 35
Hlavacek-Larrondo, J., Rhea, C. L., Webb, T., et al. 2020, ApJL, 898, L50
Hogan, M. T., Edge, A. C., Hlavacek-Larrondo, J., et al. 2015, MNRAS, 453, 1201
Huang, N., Bleem, L. E., Stalder, B., et al. 2020, AJ, 159, 110
Hudson, D. S., Mittal, R., Reiprich, T. H., et al. 2010, A&A, 513, A37
Hunter, J. D. 2007, CSE, 9, 90
Kennicutt, R. C. J. 1998, ARA&A, 36, 189
Kewley, L. J., Geller, M. J., & Jansen, R. A. 2004, AJ, 127, 2002
Khullar, G., Bleem, L. E., Bayliss, M. B., et al. 2019, ApJ, 870, 7
Leitherer, C., Schaerer, D., Goldader, J. D., et al. 1999, ApJS, 123, 3
Lin, H. W., McDonald, M., Benson, B., & Miller, E. 2015, ApJ, 802, 34
McDonald, M., Allen, S. W., Bayliss, M., et al. 2017, ApJ, 843, 28
McDonald, M., Benson, B. A., Vikhlinin, A., et al. 2013, ApJ, 774, 23
McDonald, M., Bulbul, E., de Haan, T., et al. 2016a, ApJ, 826, 124
McDonald, M., Gaspari, M., McNamara, B. R., & Tremblay, G. R. 2018, ApJ, 858, 45
McDonald, M., Stalder, B., Bayliss, M., et al. 2016b, ApJ, 817, 86
McDonald, M., Veilleux, S., & Mushotzky, R. 2011, ApJ, 731, 33
McDonald, M., Veilleux, S., Rupke, D. S. N., & Mushotzky, R. 2010, ApJ, 721, 1262
McMullin, J. P., Waters, B., Schiebel, D., Young, W., & Golap, K. 2007, in ASP Conf. Ser. 376, Astronomical Data Analysis Software and Systems XVI, ed. R. A. Shaw, F. Hill, & D. J. Bell (San Francisco, CA: ASP), 127
McNamara, B. R., & Nulsen, P. E. J. 2007, ARA&A, 45, 117
McNamara, B. R., & Nulsen, P. E. J. 2012, NJPh, 14, 055023
Moustakas, J., Kennicutt, R. C. J., & Tremonti, C. A. 2006, ApJ, 642, 775
Mushotzky, R. F., & Loewenstein, M. 1997, ApJL, 481, L63
Nurgaliev, D., McDonald, M., Benson, B. A., et al. 2017, ApJ, 841, 5
O'Dea, C. P., Baum, S. A., Privon, G., et al. 2008, ApJ, 681, 1035
Peterson, J. R., & Fabian, A. C. 2006, PhR, 427, 1
Peterson, J. R., Kahn, S. M., Paerels, F. B. S., et al. 2003, ApJ, 590, 207
Planck Collaboration, Ade, P. A. R., Aghanim, N., et al. 2016, A&A, 594, A27
Qiu, Y., Bogdanović, T., Li, Y., Park, K., & Wise, J. H. 2019, ApJ, 877, 47
Rafferty, D. A., McNamara, B. R., Nulsen, P. E. J., & Wise, M. W. 2006, ApJ, 652, 216
Rosa-Gonzalez, D., Terlevich, E., & Terlevich, R. 2002, MNRAS, 332, 283
Ruppin, F., McDonald, M., Bleem, L. E., et al. 2021, ApJ, 918, 43
Ruppin, F., McDonald, M., Hlavacek-Larrondo, J., et al. 2022, arXiv:2207.13351
Sanders, J. S., Fabian, A. C., Russell, H. R., & Walker, S. A. 2018, MNRAS, 474, 1065
Santos, J. S., Tozzi, P., Rosati, P., Nonino, M., & Giovannini, G. 2012, A&A, 539, A105
Sault, R. J., Teuben, P. J., & Wright, M. C. H. 1995, in ASP Conf. Ser. 77, Astronomical Data Analysis Software and Systems IV, ed. R. A. Shaw, H. E. Payne, & J. J. E. Hayes (San Francisco, CA: ASP), 433
Somboonpanyakul, T., McDonald, M., Gaspari, M., Stalder, B., & Stark, A. A. 2021, ApJ, 910, 60
Strazzullo, V., Pannella, M., Mohr, J. J., et al. 2019, A&A, 622, A117
Sunyaev, R. A., & Zeldovich, Y. B. 1972, CoASP, 4, 173
Sutherland, R. S., & Dopita, M. A. 1993, ApJS, 88, 253
Urban, O., Werner, N., Allen, S. W., Simionescu, A., & Mantz, A. 2017, MNRAS, 470, 4583
van der Walt, S., Colbert, S. C., & Varoquaux, G. 2011, CSE, 13, 22
Vikhlinin, A., Kravtsov, A., Forman, W., et al. 2006, ApJ, 640, 691
Voit, G. M., Kay, S. T., & Bryan, G. L. 2005, MNRAS, 364, 909
Webb, T. M. A., Muzzin, A., Noble, A., et al. 2015, ApJ, 814, 96
Willingale, R., Starling, R. L. C., Beardmore, A. P., Tanvir, N. R., & O'Brien, P. T. 2013, MNRAS, 431, 394